Characteristics of low-aspect ratio, large-diameter, high-density helicon plasmas with variable axial boundary conditions

T. Motomura, S. Shinohara, T. Tanikawa, and K. P. Shamrai

Citation: Phys. Plasmas 19, 043504 (2012); doi: 10.1063/1.3701558
View online: http://dx.doi.org/10.1063/1.3701558
View Table of Contents: http://pop.aip.org/resource/1/PHPAEN/v19/i4
Published by the American Institute of Physics.

Characteristics of low-aspect ratio, large-diameter, high-density helicon plasmas with variable axial boundary conditions

T. Motomura,[1] S. Shinohara,[2] T. Tanikawa,[3] and K. P. Shamrai[4]
[1]*Interdisciplinary Graduate School of Engineering Sciences, Kyushu University, Kasuga, Fukuoka 816–8580, Japan*
[2]*Institute of Engineering, Tokyo University of Agriculture and Technology, Koganei, Tokyo 184–8588, Japan*
[3]*Research Institute of Science and Technology, Tokai University, Hiratsuka, Kanagawa 259–1292, Japan*
[4]*Institute for Nuclear Research, National Academy of Sciences, Kiev 03680, Ukraine*

(Received 22 November 2011; accepted 20 March 2012; published online 6 April 2012)

A low-aspect ratio, high-density helicon plasma source with a large-diameter of ~74 cm that utilizes an end-launch flat-spiral antenna has been characterized under three different axial boundary conditions. Whereas one end of the device is a quartz-glass window through which an excitation rf wave is injected, the other end is a movable plasma terminating plate of three different kinds: (1) metal with small holes, (2) solid metal, and (3) solid insulator. Using this movable plate, the device aspect ratio A (device axial length/device diameter) can be reduced to ~0.075 corresponding to the device axial length of 5.5 cm. The plasma production efficiency (PPE, defined as the ratio of the total number of electrons in the plasma to the input rf power) and helicon wave structures are examined for plasmas with various aspect ratios and boundary conditions to characterize our helicon device. Even for the lowest aspect ratio case (A ~0.075), a plasma with the electron density of 7.5×10^{11} cm^{-3} can be produced. The PPE of our device is higher than that of other helicon devices that utilize winding-type antennas. Discrete axial wave modes, which can be explained by a simple model, have been identified for helicon waves excited in our low-aspect ratio helicon plasmas. A comparison between the experimental results and helicon wave theory suggests that second order radial modes must have been excited when the electron density is sufficiently high. © *2012 American Institute of Physics*. [http://dx.doi.org/10.1063/1.3701558]

I. INTRODUCTION

Plasmas can be produced very efficiently by using helicon waves, or whistler waves propagating in a bounded plasma region, whose frequency is $\omega_{ci} \ll \omega \ll \omega_{ce}$, where ω_{ci} and ω_{ce} are the ion- and electron-cyclotron frequencies, respectively.[1–4] Because it is possible to easily obtain high-density (~10^{13} cm^{-3}) plasmas with high ionization rate (several tens of percent) under a wide range of magnetic field strength in helicon-wave discharge, helicon plasma sources are suitable for various plasma applications, such as basic science experiments,[5–7] developing magnetoplasma rocket engines,[8,9] plasma processings,[10,11] and fusion related experiments.[12]

A low-aspect ratio plasma source with uniform density profile is especially useful for such applications like plasma processings and plasma thrusters. Here, the aspect ratio A of the device is defined as the ratio of the effective axial length (in our case, the distance between one end of the chamber and the plasma terminating plate, see Sec. III) to the device diameter. In plasma thruster application, for example, the thrust can be increased by simply increasing the plasma diameter. Therefore, using a low-aspect ratio plasma source with a large-diameter is very advantageous so as to decrease the overall thruster size and cost. In addition, there must be an optimum way to axially terminate the plasma for each application. For instance, the axial boundary should be an insulator for the production of thin-solid films in a plasma processing field.[11] If one wants to construct an ion source (an ion thruster is one), the axial termination plate can be a metal plate with small holes or a metal grid so as to extract ions out of the plasma source region. The above two points have motivated us to perform our current research of low-aspect ratio, large-diameter helicon plasmas with various axial boundary conditions.

In our previous research, high-density helicon plasmas have been characterized using the Large Helicon Plasma Device (LHPD, ~74 cm in inner diameter and 486 cm in device length) at the Institute of Space and Astronautical Science, a division of the Japan Aerospace Exploration Agency (ISAS/JAXA).[13–16] The LHPD has been converted into a low-aspect ratio helicon plasma source by installing a movable plasma terminating plate inside the vacuum chamber in order to effectively shorten the plasma axial length.[17,18] The lowest aspect ratio achievable is A ~0.075. Previously, the experiment with a low-aspect ratio helicon plasma source of A ~0.5 was conducted using an end launch antenna and a wafer platen.[19] In another example, using a single loop antenna and a conductor plate, helicon plasma characteristics were studied in a short axial length device (down to 10 cm, $A > 2$).[20] However, as far as we know, the characteristics of helicon plasmas produced with a low-aspect ratio device of $A < 0.5$ have not been fully investigated yet.

In this research, the characteristics of low-aspect ratio helicon plasmas ($0.075 \leq A \leq 6.6$) are successively studied by using three different types of termination plates to shorten the effective plasma length: (1) a metal plate with small holes, (2) a solid metal plate, and (3) a solid insulator plate. The radial and axial profiles of the axial component of the

excited rf magnetic field were measured in order to investigate the characteristics of excited helicon waves.

The outline of this paper is as follows: In Sec. II, the general theory and our definitions regarding helicon waves in a low-aspect ratio helicon plasma source are described. In Sec. III, the experimental setup and diagnostics used are described. In Sec. IV, the experimental results for various aspect ratio cases ($0.075 \leq A \leq 6.6$) of large-diameter, high-density helicon plasmas are presented for three different axial boundary conditions under various input rf powers and magnetic field configurations. Some discussions regarding the results are also given. Finally, a concluding summary is given in Sec. V.

II. THEORIES OF HELICON PLASMAS

In this section, we describe (A) the dispersion relation of a helicon wave with $m=0$ azimuthal mode in a uniform plasma and the expressions for the excited rf magnetic and electric fields associated with the wave, (B) the axial mode number of a standing-type helicon wave excited in a low-aspect ratio helicon plasma, and (C) the plasma production efficiency in a low-aspect ratio helicon plasma.[14]

A. Theories for helicon waves in plasmas with uniform electron density under a uniform magnetic field

For a cylindrical plasma immersed in a uniform dc magnetic field, the basic equations for the helicon wave fields can be given by[21]

$$\nabla \times \mathbf{E} = -\frac{\partial \mathbf{B}}{\partial t}, \tag{1}$$

$$\nabla \times \mathbf{B} = \mu_0 \mathbf{j}, \tag{2}$$

and

$$\mathbf{E} = \frac{\mathbf{j} \times \mathbf{B}_0}{e n_0}, \tag{3}$$

where $\mathbf{E}$, $\mathbf{B}$, and $\mathbf{j}$ are the small perturbations of the electric field, the magnetic field, and the plasma current, respectively, e is the elementary charge, n_0 is the unperturbed background plasma density, and $\mathbf{B}_0 = B_0 \hat{z}$ is the axial dc magnetic field, where $\hat{z}$ stands for the unit vector in the axial direction. Under a normal approximation for the helicon plasma conditions, $\omega_{pe} \gg \omega_{ce}$ (ω_{pe}: the electron plasma frequency), the displacement current can be neglected in Eq. (2). However, this does not exclude the slow (Trivelpiece-Gould) wave solution. Equation (3) is derived from the equation of motion for electrons in the so-called helicon approximation. Here, the $\mathbf{E} \times \mathbf{B}$ drift is retained, whereas the polarization drift is neglected; this does exclude the slow waves. Generally speaking, the inclusion of the slow waves is needed for an adequate interpretation of experiments (e.g., Ref. 22), but it is not the case for our experiments discussed below. Indeed, quasi-potential slow waves are not directly excited by the antenna, in contrast to electromagnetic helicon waves and can arise only through two kinds of the mechanism for the mode conversion of helicon waves.[23] The mechanism of the first kind is the surface mode conversion that occurs due to the abrupt plasma edge polarization near the radial wall of an insulating chamber. This mechanism is invalid for our experiment where the plasma is confined in a metal chamber, contrary to an insulating chamber as in standard helicon sources (e.g., Ref. 22). Also, the plasma density is very low near the chamber wall. The mechanism of the second kind is the bulk mode conversion that occurs when the condition for the coalescence of the helicon and slow waves, $k_z < 2(\omega/c)(\omega_{pmax}/\omega_{ce})$ (ω_{pmax}: the maximum plasma frequency at the center),[23] is satisfied. Under this condition, helicon waves are peripherally localized and do not appear near the plasma center. As long as all waveforms observed in our experiments are centrally localized, the mechanism of bulk mode conversion is apparently invalid. Thus, the helicon approximation, which ignores the slow waves, is quite adequate for the interpretation of our experimental data.

If the first order wave quantities are assumed to follow the form $\exp[i(m\theta + k_\parallel z - \omega t)]$, where m is the azimuthal mode number, θ is the azimuthal angle, $k_\parallel$ is the parallel wavenumber, and ω is the wave frequency, the axial component of the wave magnetic field $\tilde{B}_z$ can be derived from the following partial differential equation[21]

$$\frac{\partial^2 \tilde{B}_z}{\partial r^2} + \frac{1}{r}\frac{\partial \tilde{B}_z}{\partial r} + \left(\alpha^2 - k_\parallel^2 - \frac{m^2}{r^2}\right)\tilde{B}_z = 0, \tag{4}$$

where $\alpha \equiv \omega\omega_{pe}^2/(k_\parallel \omega_{ce} c^2)$ and c is the speed of light. Here, the perpendicular wavenumber $k_\perp$ can be defined by

$$k_\perp^2 = \alpha^2 - k_\parallel^2. \tag{4'}$$

This relation actually gives rise to the dispersion relation for helicon waves with the $m=0$ azimuthal mode,

$$k_\parallel^2(k_\parallel^2 + k_\perp^2) = \left(\frac{\omega\omega_{pe}^2}{\omega_{ce}c^2}\right)^2. \tag{5}$$

The perpendicular and parallel wavenumbers depend on the strength of the background magnetic field, the electron density, and the excitation frequency via the dispersion relation, Eq. (5).

The solution for Eq. (4) is a Bessel function of the first kind of order m, $J_m(k_\perp r)$. The boundary condition is given by $\tilde{j}_r = 0$ (or $\tilde{B}_\theta = 0$) at the insulating radial boundary and by $\tilde{E}_\theta = 0$ (or $\tilde{B}_r = 0$) at the conducting radial boundary. For $m=0$ mode, the boundary condition for both cases can be written as

$$J_1(k_{\perp j} a) = 0. \tag{6}$$

Here, $k_{\perp j} a$ gives the jth root of J_1, $k_{\perp j}$ can be treated as the jth order perpendicular wavenumber, and a is the effective plasma radius.

For a cylindrical plasma with an infinite axial length, the excited rf magnetic and electric fields associated with the $m=0$ helicon wave[21] can be expressed by

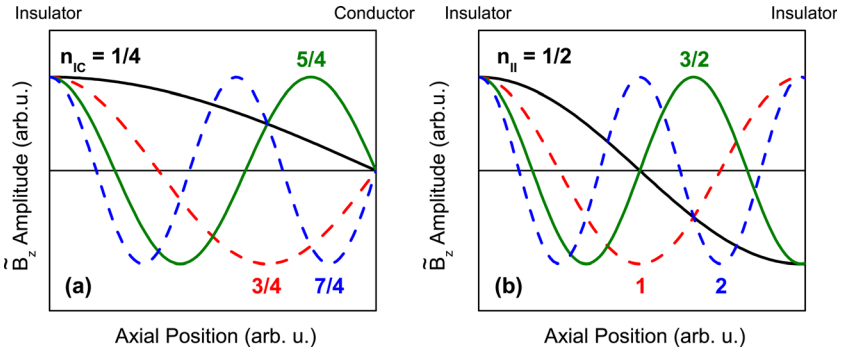

FIG. 1. Idealized helicon wave patterns of $\tilde{B}_z$ in low-aspect ratio helicon plasmas. Cases for two different axial boundary conditions are depicted: (a) Insulator (left-hand boundary)-Conductor (right-hand boundary) case [see Eq. (10)] and (b) Insulator (left-hand boundary)-Insulator (right-hand boundary) case [see Eq. (11)].

$$\tilde{B}_r = -Ck_{\|}J_1(k_{\perp j}r)\cos(k_{\|}z-\omega t),$$
$$\tilde{E}_r = C\omega(\alpha/k_{\|})J_1(k_{\perp j}r)\sin(k_{\|}z-\omega t), \quad (7)$$

$$\tilde{B}_\theta = C\alpha J_1(k_{\perp j}r)\sin(k_{\|}z-\omega t),$$
$$\tilde{E}_\theta = C\omega J_1(k_{\perp j}r)\cos(k_{\|}z-\omega t), \quad (8)$$

$$\tilde{B}_z = Ck_{\perp j}J_0(k_{\perp j}r)\sin(k_{\|}z-\omega t), \quad \tilde{E}_z = 0, \quad (9)$$

where C is a constant. We note that, in order to derive more realistic wave field profiles, damping effects,[21] such as the damping lengths of the Landau damping L_{LD} and the elastic collisions L_{coll}, must be taken into account.

B. Helicon wave fields in a short axial length plasma

For a short axial length helicon plasma, the axial structure of helicon wave is strongly affected by the presence of axial boundaries, and the wave is essentially a standing-type.[17,18,20,24] Experimentally, the wave amplitude always becomes zero (node) at a conductor boundary, whereas that becomes local maximum (anti-node) at an insulator boundary. These results are consistent with the following wave boundary conditions: $\tilde{B}_z = 0$ at a conductor while $\partial\tilde{B}_z/\partial z = 0$ (and $\tilde{B}_z \neq 0$) at an insulator. In our experiments, one of the ends is always an insulator [i.e., the quartz-glass window for the wave launching antenna, see Fig. 2(a)], whereas another end (a plasma terminating plate) is either a conductor or an insulator. When the termination plate is a conductor, provided that the effect of surface waves near boundaries is negligible, we can obtain $L_p = (1/4 + l/2)\lambda_{\|l}(l = 0, 1, 2, \ldots)$, where L_{p} and $\lambda_{\|l}$ are the plasma length and the lth parallel wavelength of the helicon wave, respectively [see Fig. 1(a)]. Then, we can define the axial mode number, n_{IC}, as

$$n_{\mathrm{IC}} = \frac{L_{\mathrm{p}}}{\lambda_{\|l}} = \frac{1+2l}{4} \quad (l = 0, 1, 2, \ldots). \quad (10)$$

Similarly, if the termination plate is an insulator, we have $L_p = (1/2 + l/2)\lambda_{\|l}(l = 0, 1, 2, \ldots)$, [see Fig. 1(b)]; then, the axial mode number n_{II} can be defined by

$$n_{\mathrm{II}} = \frac{L_{\mathrm{p}}}{\lambda_{\|l}} = \frac{1+l}{2} \quad (l = 0, 1, 2, \ldots). \quad (11)$$

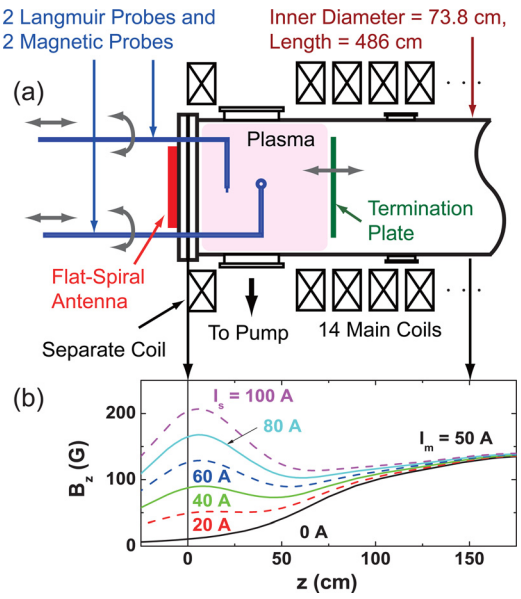

FIG. 2. Experimental configuration. (a) Schematic drawing of the LHPD at ISAS/JAXA. Only the portion used for low-aspect ratio experiments is shown. (b) Axial profiles of the background dc magnetic field, B_z, for various values of the separate coil current I_{s}. The main coil current I_{m} is fixed at 50 A.

C. Plasma production efficiency of a low-aspect ratio helicon plasma

Using the definition of the plasma production efficiency (PPE, defined as the ratio of the total number of electrons in the plasma to the input rf power) in Ref. 14, the PPE of low-aspect ratio helicon plasmas has been examined in our experiments. In general, a steady-state plasma production is a result of the balance between the plasma loss and generation. If the plasma loss is dominated by the ambipolar diffusion, the ion diffusion mainly determines the actual plasma loss. If the ions are magnetized by the axial magnetic field and the device has a short axial length with a large-diameter, the plasma production efficiency can be restricted by the axial ion loss. Then, the input rf power P_{inp} is balanced by the outgoing energy flux of $2\pi R^2 W n_{\mathrm{s}} C_{\mathrm{s}}$ along the axial magnetic field lines toward the both ends of the chamber. Here, R is the device radius, W is the mean energy to produce an ion-electron pair, $n_s = f\,\bar{n}_{\mathrm{e}}$ is the electron density at the sheath edge, f is a numerical factor, $\bar{n}_{\mathrm{e}}$ is the average bulk electron density, and C_{s} is the Bohm velocity. Introducing the total number of electrons in the device, $N_{\mathrm{e}} = \bar{n}_{\mathrm{e}}\pi R^2 L$, where L is the device length, we obtain the PPE as

$$\mathrm{PPE} = \frac{N_e}{P_{inp}} = \frac{L}{2WC_s f}. \quad (12)$$

If we adopt the following numerals: $f = 0.2$, $T_i = 0.05$ eV, $T_e = 3$ eV, and $W = 70$ eV, then, using Eq. (12), we obtain $\mathrm{PPE} = N_e/P_{inp} \sim 0.1L$ (cm) $(10^{13}\,\mathrm{W}^{-1})$.[14] On the other hand, the PPE is proportional to R^2 in the long axial length case (high-aspect ratio case), since the radial plasma loss is dominant in this case.[14] Thus, using measured density profile we can estimate the PPE's for plasmas with various axial lengths applying the above simple scaling.

III. EXPERIMENTAL SETUP AND DIAGNOSTIC TECHNIQUES

Figure 2(a) shows the LHPD at ISAS/JAXA whose inner diameter and axial length are 73.8 cm and 486 cm, respectively. The external dc magnetic field is produced by the 14 main coils and the separate coil whose left edge coincides with the axial position of $z = 0$. The 4-turn flat spiral antenna,[13] ~43 cm in diameter, is connected to an rf power supply [maximum output power of 5 kW (in a pulsed mode) with 7 MHz excitation frequency] through a matching box that utilizes a split tank circuit. The antenna is expected to launch waves with the $m = 0$ azimuthal mode. The magnetic field configuration in the plasma generation region can be varied by controlling the separate coil current I_s as shown in Fig. 2(b).

A movable plasma terminating plate is installed inside the vacuum chamber in order to limit the axial plasma length. The terminating plate is electrically floating and its position, z_E, is adjustable between 5.5 cm and 125 cm. Three different kinds of terminating plates were used in our experiments: (1) a stainless steel plate (the diameter ~54 cm) with small holes (the hole diameter = 1.5 mm, the center-to-center separation of neighboring holes = 3 mm, and the geometrical transparency ~35 %), (2) a solid stainless steel plate (the diameter ~54 cm), and (3) a solid insulator (mica) plate (the diameter ~50 cm). The working gas was argon with a fill pressure p_{Ar} of 0.75 mTorr unless otherwise stated. A typical electron temperature was T_e ~3 eV, which is consistent with the previous results obtained in the LHPD.[13]

Two magnetic probes are used to measure the axial component of the excited rf magnetic field, $\tilde{B}_z$. Two Langmuir probes are used to measure the spatial profiles of the ion saturation current from which the electron density is deduced. Their probe shafts are inserted into the plasma from the end flange of the antenna side and are bent into an L-shape so that the probes can radially scan the plasma [a scannable radial (or horizontal) range is $x = -35$ ~35 cm] by rotating the probe shafts. They are also axially movable: $z = 0.5$ ~80 cm. Each magnetic probe consists of a one-turn loop with oval shape, ~13 mm in long axis and ~8 mm in short axis. One of the Langmuir probes is a cylindrical type (0.8 mm in diameter and 3 mm in length) and the other is a one sided disc type (3 mm in diameter). The Langmuir probes are negatively biased so as to measure the ion saturation current whose value is used to estimate the electron density n_e. Although we did not make extensive measurements of the electron temperature T_e profiles, the estimated error due to the T_e variation in determining n_e from the measured ion saturation current is within ~20% based on the previous results of $T_e = 3 - 5$ eV. We note that T_e tends to be lower in the outer region of the plasma than in the central region where a typical value of T_e is ~3 eV.

For measurements of the spatial profiles of the axial component of the excited rf magnetic field, $\tilde{B}_z$, the rf antenna current, $\tilde{I}_A$, is used as a reference signal: the relative amplitude and the phase of $\tilde{B}_z$ with respect to $\tilde{I}_A$, *i.e.*, $|\tilde{B}_z|/|\tilde{I}_A|$ and φ_{rel}, are measured. For the measurement of the antenna current, we use a current probe (Pearson 6600) in the matching box. The input rf power P_{inp} to the plasma is defined as $P_{for} - P_{ref}$, where P_{for} and P_{ref} are the forward and reflected rf powers, respectively. The ratio of the reflected rf power to the forward rf power, P_{ref}/P_{for}, is typically much less than 0.2.

IV. EXPERIMENTAL RESULTS AND DISCUSSIONS

A. Electron density n_e vs. input rf power P_{inp} for various axial lengths and boundaries

Before presenting the characteristics of helicon plasmas with short axial length, we show the results of the electron density n_e as a function of the input rf power P_{inp} for plasmas with the full axial length (486 cm, corresponding to the aspect ratio A of ~6.6) in Fig. 3.[17] The data for each frame in

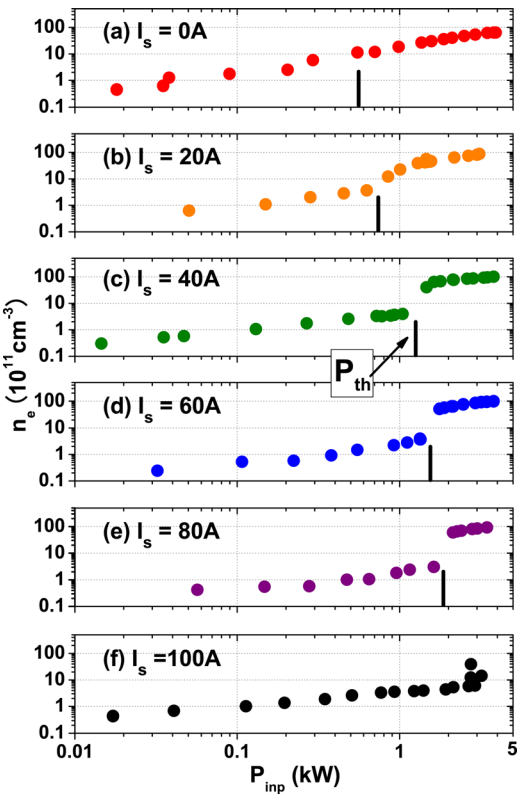

FIG. 3. Electron density n_e as a function of the input rf power P_{inp} for the full axial length (486 cm) case.[17] The separate coil current I_s is varied from 0 A to 100 A, effectively changing the degree of convergence of the background magnetic field near the antenna region. The Langmuir probe that monitored n_e was located at $x = 7.5$ cm and $z = 31.5$ cm.

Fig. 3 was taken for the different magnetic field configurations [as shown in Fig. 2(b)] realized by varying the separate coil current I_s. We note that increasing in I_s alters the magnetic field configuration near the antenna from a convergent pattern to a divergent one. It should be pointed out that the end flange of the vacuum vessel is made of stainless steel and no plasma terminating plate to limit the plasma length was installed for this series of measurements. The Langmuir probe to monitor the electron density was located at $x = 7.5$ cm and $z = 31.5$ cm. The vertical bar in each frame indicates the threshold power P_{th} at which the density jump from an inductively coupled plasma (ICP) (Ref. 25) to a helicon plasma (HP) occurs. When the density jump was not clear, the threshold power was estimated by monitoring the abrupt change in the plasma impedance. It can be seen that the electron density reaches $\sim 10^{13}$ cm^{-3} in the high-density HP discharge regime. It can also be seen that the threshold power P_{th} increases (at the same time the position of P_{th} becomes clearer and easier to identify) as the separate coil current I_s is increased (i.e., the magnetic field strength near the antenna becomes larger) up to 80 A. Further increase in I_s (to 100 A) suppresses the density jump for $P_{inp} \leq 4$ kW. Our finding that the value of P_{th} increases with the increase in I_s (i.e., with the increase in the magnetic field strength near the antenna) differs from that by Keiter *et al.*[26] who observed that P_{th} decreases with the increase in the magnetic field strength. However, it seems inappropriate to contrast these findings because the experimental conditions for two experiments are substantially different from each other. First, Keiter *et al.*'s experiment[26] was performed with a standard helicon source excited radially by using a shell-type antenna wound around a dielectric chamber, whereas in our experiment, the source was excited axially, by a planar (or flat-spiral) antenna located outside the dielectric window at one of the ends. Second, Keiter *et al.*[26] observed the density jumps at high magnetic fields only, $\geq$500 G, whereas in our experiments the magnetic field strength near the antenna was $\lesssim$ 200 G in all cases. Finally, Keiter *et al.*'s experiments[26] were carried out in uniform magnetic field configurations, whereas we used considerably non-uniform magnetic field configurations in our experiments. Just the latter circumstance seems to be decisive and enables qualitative explanation of our results in the following way. It was found for a large-scale helicon plasma[27,28] that if the magnetic field lines under the antenna are inclined to the dielectric wall surface (or to the surface of the window at one of the ends in our case) at an angle θ exceeding the resonance group velocity angle, $\theta > \theta_{gr} = \sin^{-1}(\omega/\omega_{ce})$, the rf power goes from the antenna into the plasma almost along the magnetic field lines. In our experiments, this condition is satisfied in the whole range of I_s variation. The magnetic field lines are most convergent from the antenna to the center of the chamber at $I_s = 0$; with increasing I_s, the degree of convergence decreases and changes to divergence at $I_s > 20$ A, as is clear from Fig. 2(b). Consequently, the power deposition is most concentrated near the axis at $I_s = 0$, which apparently makes the density jump possible at lowest input power P_{th} and spreads out of the axis with increasing I_s, which postpones the jump to a higher P_{th}.

Interestingly, however, Shinohara and Yonekura[29] found that the behavior of the density jump is quite similar to ours in a wide range of uniform magnetic field (0 $\sim$1 kG) even with the use of a double loop antenna. According to a theoretical consideration by Shinohara and Shamrai,[30] this is attributable to the fact that the argon fill pressure in the experiments performed by Shinohara and Yonekura[29] was rather high ($\sim$50 mTorr).

Next, the experimental results obtained for plasmas with a plasma terminating plate installed inside the vacuum vessel to shorten the effective plasma length are shown. The axial position of the plate z_E was variable, and three different types of plates were used (as is described in Sec. III) for the measurements.

Figure 4 shows the electron density n_e as a function of the input rf power P_{inp} for the cases of three different axial lengths [(a) $z_E = 54.5$ cm, (b) $z_E = 34.5$ cm, and (c) $z_E = 5.5$ cm]. The conductor plate with small holes was used as a plasma terminating plate. The position of the Langmuir probe was at ($x = 0$ cm, $z = 25$ cm) for the $z_E = 54.5$ cm case, at ($x = 0$ cm, $z_p = 15$ cm) for the $z_E = 34.5$ cm case, and at ($x = 0$ cm, $z \sim 4$ cm) for the $z_E = 5.5$ cm case. Similar to the full length plasma case, even for the shorter axial length cases [except for the shortest ($z_E = 5.5$ cm) case with $p_{Ar} = 1.5$ mTorr], the density jump is observed, and the value of P_{th} tends to increase as I_s is increased. For the shortest ($z_E = 5.5$ cm) plasma case [see Fig. 4(c)], the density jump

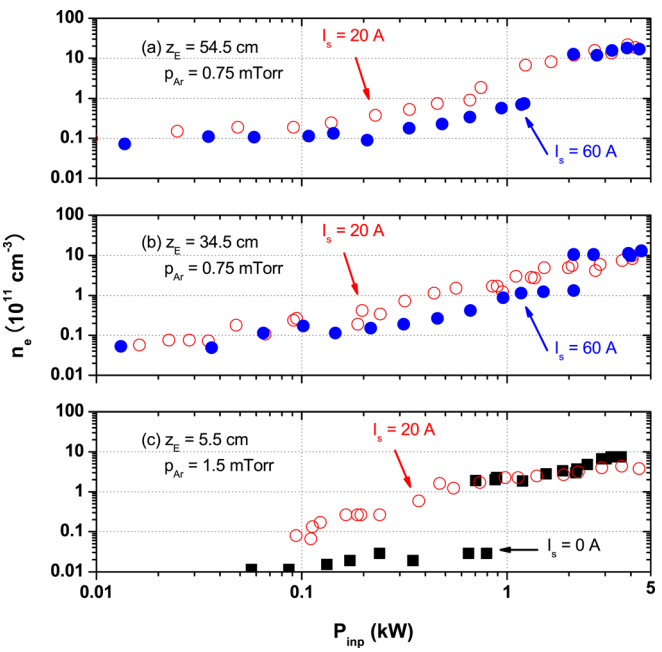

FIG. 4. Several examples of the electron density, n_e, as a function of the input rf power P_{inp} for low-aspect ratio plasmas ($A \sim 0.075$, 0.47, and 0.74). The device aspect ratio was changed by varying the position of the plasma terminating plate (a conductor plate with small holes), z_E. In Fig. 4(b), the open and closed circles are the data taken for the $I_s = 20$ A and 60 A cases, respectively.[17] In Fig. 4(c), the open circles and the closed squares show the data taken for the $I_s = 20$ A and 0 A cases, respectively. The argon gas pressures p_{Ar} used are 0.75 mTorr for Figs. 4(a) and 4(b) and 1.5 mTorr for Fig. 4(c). The Langmuir probe to monitor n_e was located at the center ($x = 0$ cm). The axial positions of the probe for Figs. 4(a) and 4(c) are at $z = 25$ cm, 15 cm, and $\sim$ 4 cm, respectively.

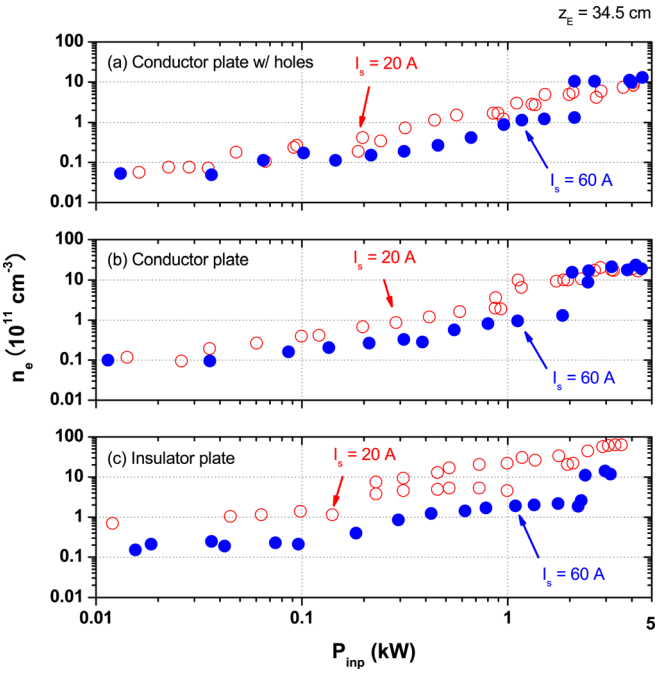

FIG. 5. Electron density n_e as a function of the input rf power P_{inp} for three different kinds of plasma terminating plate: (a) a conductor plate with small holes,[17] (b) a solid conductor plate, and (c) a solid insulator plate. The axial position of the plasma terminating plate is fixed at $z_E = 34.5$ cm ($A \sim 0.47$). The open and closed circles show the data taken for the $I_s = 20$ A and 60 A cases, respectively. The Langmuir probe to monitor n_e was located at $x = 0$ cm and $z = 15$ cm.

is observed for $I_s = 0$ A with a higher neutral gas pressure (1.5 mTorr).

Figure 5 shows the electron density n_e as a function of the input rf power P_{inp} for three different axial boundary conditions realized using three different plasma terminating plates: (a) a conductor plate with holes, (b) a solid conductor plate, and (c) a solid insulator plate. The plate position for all three cases was $z_E = 34.5$ cm. The Langmuir probe was located at $x = 0$ cm and $z = 15$ cm. For all cases, the position of P_{th} is easier to identify for larger I_s. The behavior is similar to those observed in Figs. 3 and 4. The maximum n_e attained after the density jump exceeds 10^{12} cm^{-3} for all boundary cases. In the region of the HP discharge at $I_s = 20$ A, it can be seen that the peak electron density increases significantly from Figs. 5(a)–5(c), indicating the axial boundary dependence of discharge characteristics. This tendency can be seen more clearly in Fig. 6 as explained in Sec. IV B.

B. Electron density profile and plasma production efficiency

Figure 6 shows (a) the radial and (b) the axial profiles of the electron density n_e for three different axial boundaries ($z_E = 34.5$ cm and $I_s = 20$ A) in the HP discharge regime ($P_{inp} = 3 \sim 4$ kW). The radial and axial density profiles were measured at (a) $z = 15$ cm and (b) $x = 0$ cm, respectively. It can be seen that the maximum density in the case of the insulator plate is much higher than those in the other cases. The effect of nonlinear diffusion discussed in Ref. 31 might be responsible for this triangular density profile for the insulator plate case.

When we discuss the utility of a plasma source, having a good PPE, N_e/P_{inp} (see Sec. II), as well as the capability of controlling the density profile, is very important. Here, N_e can be evaluated by integrating the electron density over the plasma column, *i.e.*, $N_e = \int n(r, z)dV = \int_0^{z_E}\int_0^R n(r, z)\, 2\pi r dr dz$. When the plasma is immersed in a strong axial magnetic field and its aspect ratio is low, the dominant factor to determine the PPE is the axial plasma loss rather than the radial plasma loss (see Sec. II).[14] In such a case, the PPE is in proportion to the axial plasma length [see Eq. (12)]. Figure 7 shows the PPE as a function of the axial position of the plasma terminating plate z_E, which is a measure of the effective plasma length, for three different axial boundaries. For the data plots shown in the figure, P_{inp} is between 3 kW and 4 kW. The dependence of the PPE on the type of the axial boundary is not strong and the PPE linearly increases with the increase in z_E. We note here that the values of N_e for all three different boundary cases (with fixed z_E and P_{inp}) are approximately the same in spite of the significant difference in radial profile between the insulator and conductor boundary cases as shown in Fig. 6(a). This is because of the fact that the contribution from the central region of the plasma column to the result of integral ($N_e = \int_0^{z_E}\int_0^R n_e(r,z) 2\pi r dr dz$) is reduced in the cylindrical geometry where the volume element $dV = 2\pi r dr dz \propto r$. In addition, the electron density decreases steeply from the center to the radial wall for the insulator plate case [see Fig. 6(a)]. The dashed line is drawn to fit the experimental data, which gives PPE $= N_e/P_{inp} \sim 0.035\, z_E$(cm) ($10^{13}$ W^{-1}). This experimentally obtained PPE for a low-aspect ratio helicon plasma using a flat spiral antenna is

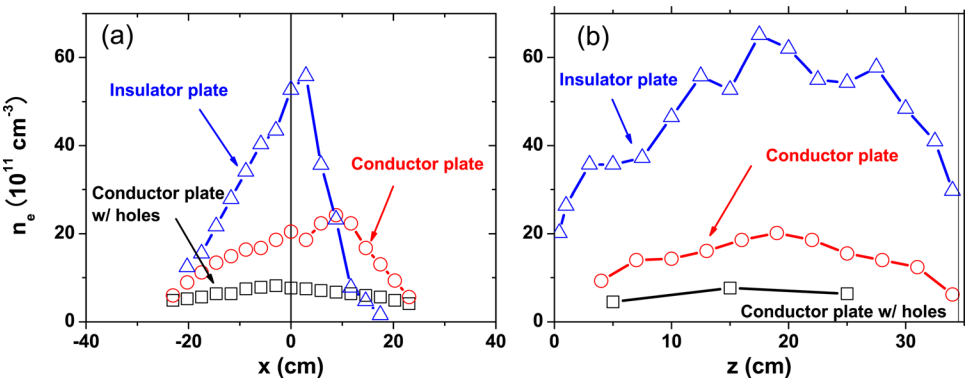

FIG. 6. Radial [(a)] and axial [(b)] profiles of the electron density n_e for three different kinds of plasma terminating plate. The position of the plasma terminating plate was $z_E = 34.5$ cm and the separate coil current was $I_s = 20$ A. The input rf power was $P_{inp} = 3 - 4$ kW. The radial profile data were taken at $z = 15$ cm, while the axial profile data were taken at $x = 0$ cm.

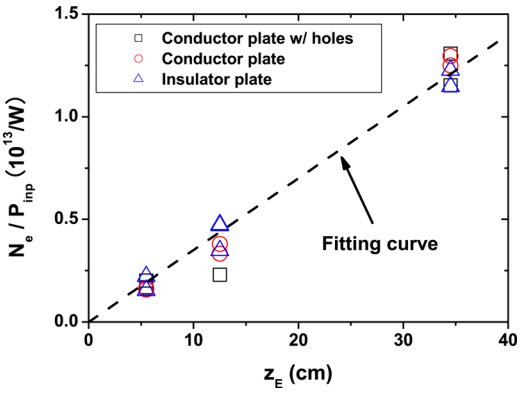

FIG. 7. PPE, N_e/P_{inp}, as a function of the axial position of the plasma terminating plate, z_E, for three different kinds of plasma terminating plate. The input rf power was $P_{inp} = 3$–4 kW. The dashed line is drawn to fit the experimental data.

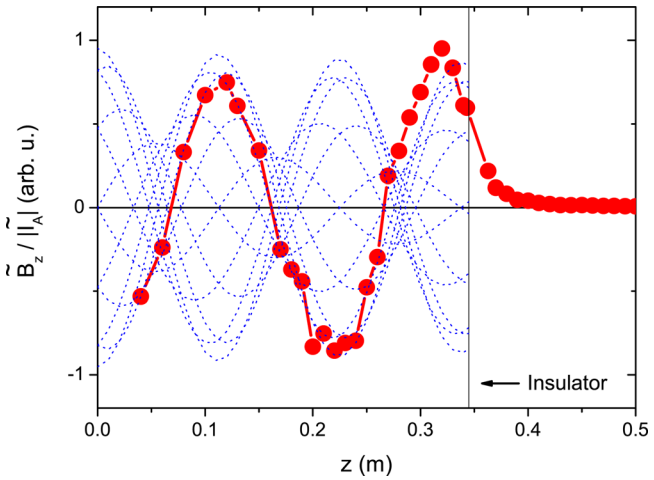

FIG. 9. Axial profile of $\sim B_z/|\sim I_A|$ $B_z/|I_A|$ for the case of a solid insulator plasma terminating plate at $z_E = 34.5$ cm with $P_{inp} \sim 3$ kW (the same experimental conditions as those used in Fig. 8). The magnetic probe was located at $x = -5.9$ cm. The red dots indicate the positions of measurements and the red curve is drawn in order to delineate the wave pattern. The blue dotted curves for $z < 34.5$ cm are drawn using Eq. (14), which models our result of a standing-type wave with damping effects. The wave reflection coefficient at the plasma terminating plate is $R \sim 0.67$ for this calculation.

smaller than the PPE estimated by using Eq. (12) by a factor of ~3. The comparison between other helicon devices[14] and the present one indicates that the value of the PPE for our device is quite high even for the cases of shorter effective axial length, $z_E \gtrsim 12.5$ cm ($A \gtrsim 0.17$), suggesting the effectiveness of using a flat spiral antenna for the production of a large-diameter plasma. Moreover, it is quite advantageous to use a flat type antenna for the production of low-aspect ratio helicon plasmas because of its easy handling and the ease of having a large-diameter plasma by simply making the antenna diameter larger.

Figure 8 shows the two-dimensional profile of the electron density in the case of the insulator plate with $z_E = 34.5$ cm at P_{inp} ~3 kW. Here, the experimental data were taken with the spatial increments of $\Delta x = \Delta z = 2$ cm. In the plasma production region, which is in the left hand side of the insulator plate, the maximum n_e is $\sim 6 \times 10^{12}$ cm^{-3}, and the axial density profile has a weak peak near the quartz-glass window in front of the antenna ($z \sim 0$ cm) and a strong peak at $z \sim 20$ cm. In order to fully understand the observed density profile, we must understand the relationship between the rf power absorption by the plasma via the helicon wave, the plasma production due to the surface wave excited by the flat type antenna, and the magnetic field configuration. This is left for the future work.

Outside the plasma production region [the right hand side of the insulator plate ($z > 34.5$ cm)], the maximum n_e is $\sim 2.5 \times 10^{11}$ cm^{-3}. The hollow radial density profile can be realized as a result of the plasma flow (or leakage) through the gap between the inner surface of the chamber and the plasma terminating plate ($|x| = 25 - 36.9$ cm, $z = 34.5$ cm). In other words, the plasma is solely produced in the left hand side of the insulator plate ($z < 34.5$ cm). The structure of the helicon wave under this electron density profile is presented in Fig. 9 (see the Sec IV C).

C. Excited rf magnetic field (the magnetic component of the helicon wave)

The radial and axial profiles of the helicon wave in a low-aspect ratio helicon plasma are measured in order to investigate the characteristics of the plasma. In this subsection, the rf magnetic field (the helicon wave) structures excited in the plasma production region are described with

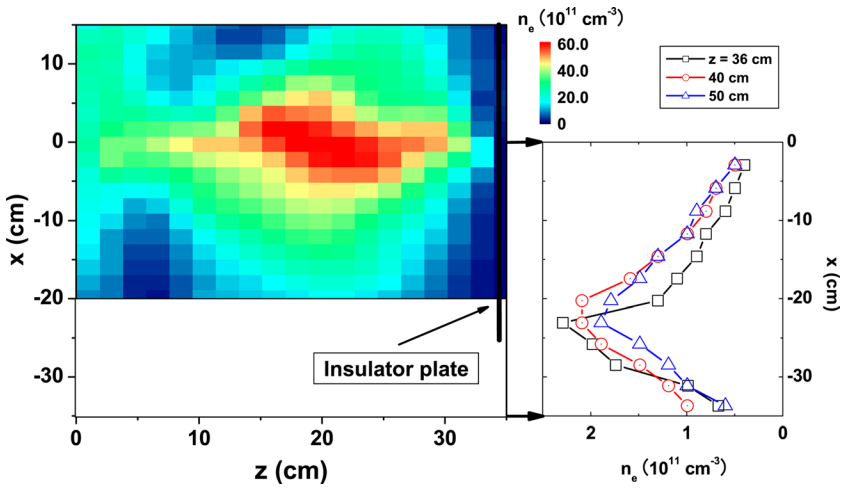

FIG. 8. Electron density, n_e, profile in the x–z plane (the figure in the left-hand side) and the radial n_e profiles at $z = 36$ cm, 40 cm, and 50 cm (the figure in the right-hand side). The plasma terminating (solid insulator) plate was located at $z_E = 34.5$ cm. The input rf power was $P_{inp} \sim 3$ kW.

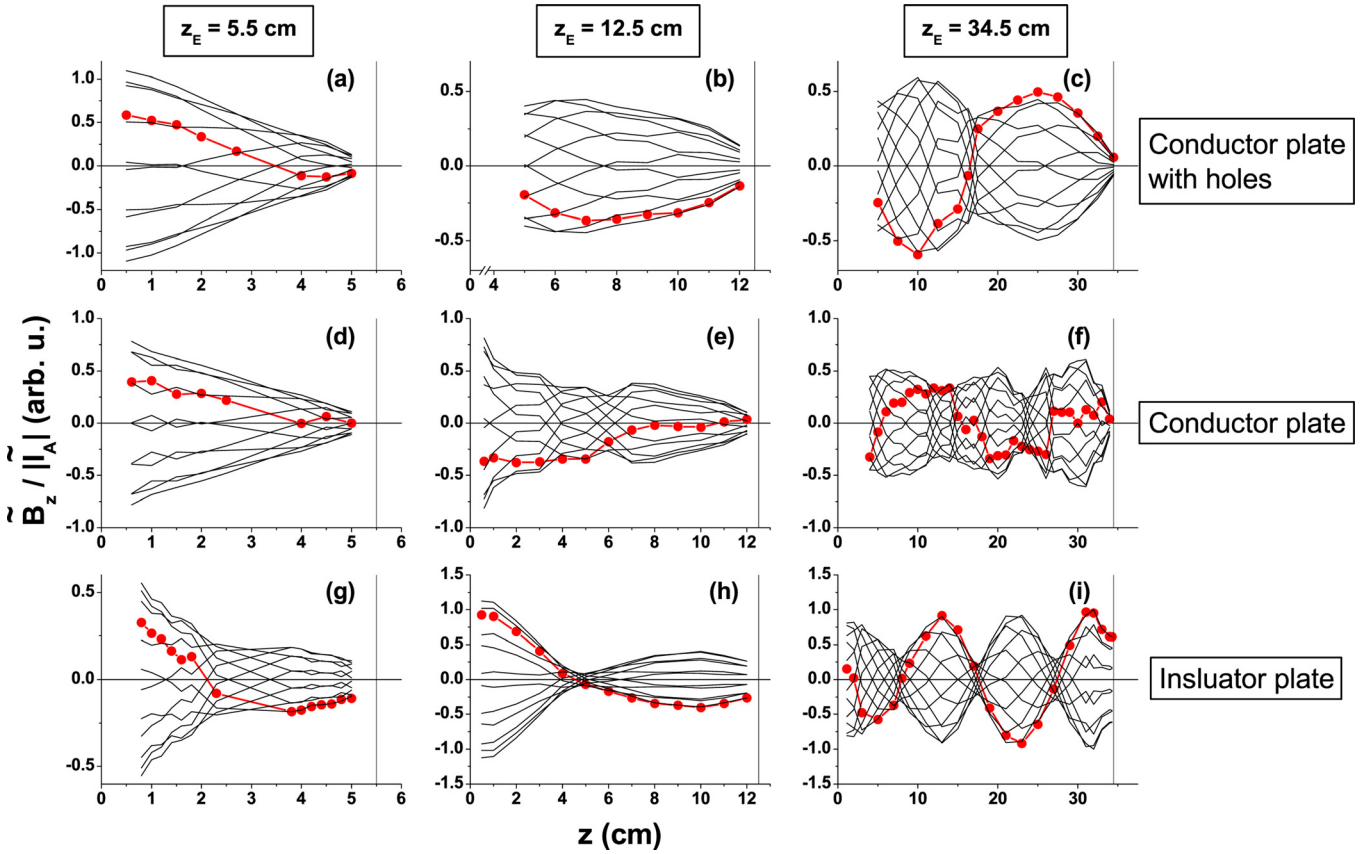

FIG. 10. Axial profiles of $\tilde{B}_z/|\tilde{I}_A|$ ($x=0$ cm) for helicon plasmas with various aspect ratios, $A \sim 0.075$, 0.17, and 0.47 (i.e., various z_E's), and different types of axial boundary condition (i.e., different types of plasma terminating plate). Twelve solid curves in each frame correspond to the spatial profiles of Eq. (13) at different t's during one rf period while the red curves with red dots correspond to the profiles of Eq. (13) at $t=0$. The input rf power used was $P_{inp}=2-4$ kW.

the effects of different axial boundary conditions and the electron density profiles.

The red curve with the red dots in Fig. 9 shows the axial profile of the excited rf wave structure measured by a magnetic probe at the radial position of $x=-5.9$ cm in Fig. 8. The axial profile of the excited rf magnetic field is derived from the amplitude $|\tilde{B}_z|/|\tilde{I}_A|$ and the phase difference φ_{rel} between the magnetic probe signal and the antenna current. Assuming simple sinusoidal oscillations with the frequency $\omega/2\pi=7$ MHz, the spatial and temporal behaviors of the wave can be described as

$$\tilde{B}_z(z,t)/|\tilde{I}_A| = (|\tilde{B}_z(z)|/|\tilde{I}_A|)\sin[\varphi_{rel}(z)+\omega t]. \quad (13)$$

The red curve in Fig. 9 corresponds to the spatial profile of Eq. (13) at $t=0$. The red dots indicate the positions of the measurements. The curve is drawn as a representative wave pattern.

As shown in Fig. 9, the observed wave structure in a low-aspect ratio helicon plasma is a standing wave type due to the effect of the wave reflections at the plasma terminating plate ($z=34.5$ cm) and the quartz-glass window of the antenna side. When both axial boundaries are insulators, a standing-type helicon wave with damping effects, $\tilde{B}_z(z,t)$, can be phenomenologically described as

$$\begin{aligned}\tilde{B}_z(z,t) = {} & A_1(z)\sin(k_\parallel z-\omega t+\phi_1)\\ & +A_2(z)\sin(-k_\parallel z-\omega t+\phi_2)\\ & +A_3(z)\sin(k_\parallel z-\omega t+\phi_3)\\ & +A_4(z)\sin(-k_\parallel z-\omega t+\phi_4), \end{aligned} \quad (14)$$

where $A_1(z)$ and ϕ_1 are the amplitude and the initial phase angle of the injected wave, and $\{A_2(z)$ and $\phi_2\}$, $\{A_3(z)$ and $\phi_3\}$, and $\{A_4(z)$ and $\phi_4\}$ are the amplitudes and the initial phase angles of the waves of successive reflections at the plasma terminating plate, the quartz-glass window, and the plasma terminating plate, respectively. The spatial dependences of all amplitudes reflect the wave damping effects. Therefore, the amplitude $A_i(z)$, where $i=1$, 2, 3, and 4, can be written as $A_i(z)=C_i\exp[-\mathrm{Im}(k_{\parallel i})z]$, where C_i is a constant, $\mathrm{Im}(k_{\parallel i})=1/L_{total}$ is an imaginary part of the axial wavenumber, and L_{total} is the total damping length as is described below. Only three successive reflections at the axial boundaries are taken into account in our calculation since the amplitudes of the waves due to further reflections become negligibly small because of the damping effects. Because we have insulator boundaries, the phase of the wave is continuous at each boundary when the wave reflects there. Since the wave can penetrate into beyond the insulator boundaries, the wave reflections at the insulator boundaries are not total reflections. From the

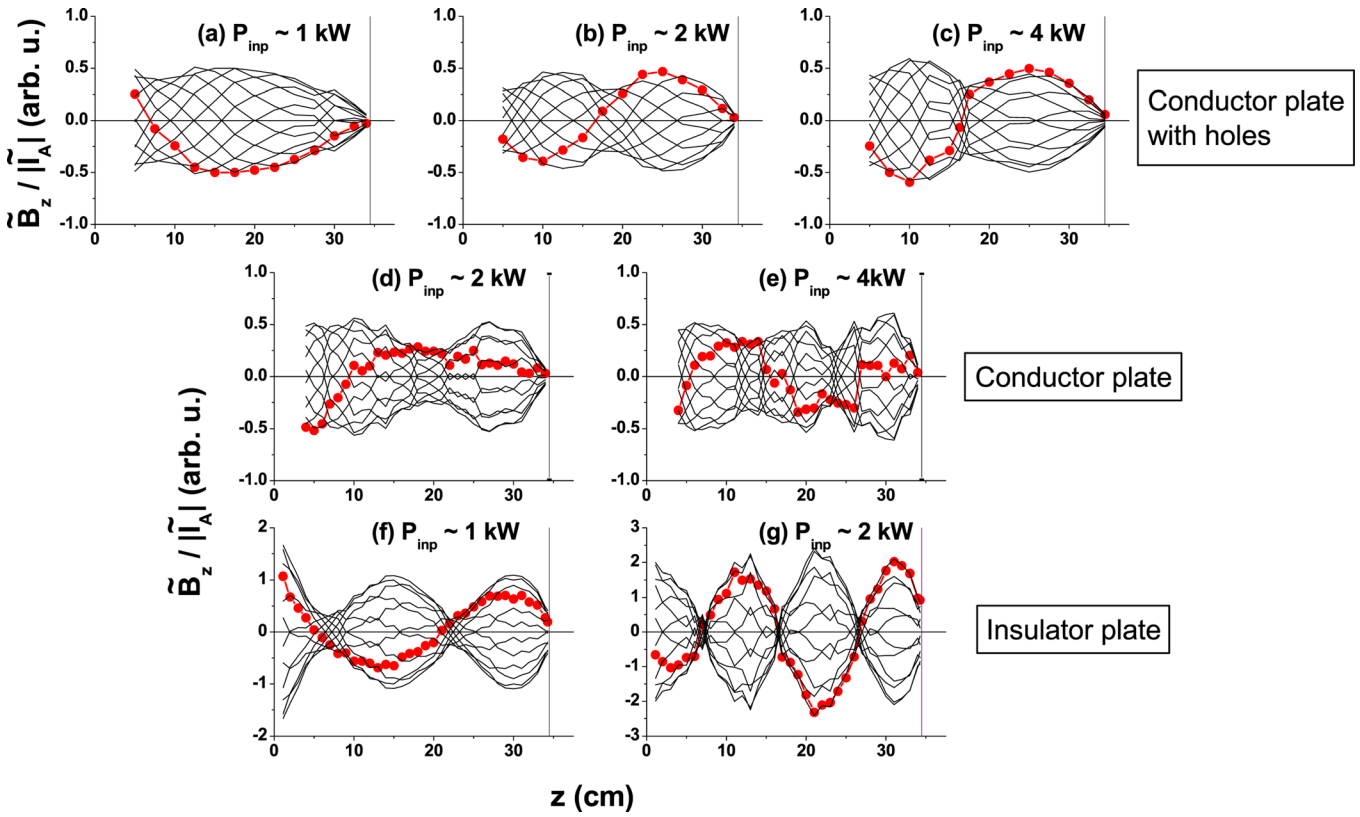

FIG. 11. Axial profiles of $\tilde{B}_z/|\tilde{I}_A|$ ($x = 0$ cm) for low-aspect ratio helicon plasmas with different values of electron density at the central plasma region, n_{ec}, under three different types of axial boundary condition. The position of the plasma terminating plate was at $z_E = 34.5$ cm ($A \sim 0.47$). The value of n_{ec} was varied by changing the input rf power P_{inp}. The thin solid curves and the red curves with red dots are drawn by the same manner to that described in Fig. 10. Plasma terminating plates used to examine the axial boundary effect were: a conductor plate with small holes [figures (a) with $P_{inp} \sim 1$ kW, (b) with $P_{inp} \sim 2$ kW, and (c) with $P_{inp} \sim 4$ kW], a solid conductor plate [figures (d) with $P_{inp} \sim 2$ kW and (e) with $P_{inp} \sim 4$ kW], and a solid insulator plate [figures (f) with $P_{inp} \sim 1$ kW and (g) with $P_{inp} \sim 2$ kW].

data we estimate the reflection coefficient as $R = A_2(z_E)/A_1(z_E) = A_3(0)/A_2(0) = A_4(z_E)/A_3(z_E) \sim 0.67$. This value is used to calculate the wave structure using Eq. (14). In order to include wave damping effects, the total damping length, $L_{total} = \mathrm{Im}(k_{\|})^{-1} = (1/L_{coll} + 1/L_{LD})^{-1}$, needs to be estimated, where L_{LD} (Ref. 21) is the damping length due to the Landau damping of the wave and L_{coll} (Ref. 21) is that due to elastic collisions between electrons and ions as well as electrons and neutrals. For the experimental conditions of Fig. 9, we find $L_{LD} \sim 1$ m and $L_{coll} \sim 5.5$ m assuming a Maxwellian electron distribution function with $T_e = 3$ eV. The resultant L_{total} is then ~ 0.8 m that is sufficiently longer than the device length. Using Eq. (14) with $L_{total} \sim 0.8$ m, the axial profiles of $\tilde{E}_z(z,t)$ are calculated and plotted in Fig. 9 (the blue dotted curves for $z < 34.5$ cm) for twelve different phases so as to clarify the temporal variations due to rf oscillations. Here, the wave amplitude is normalized by the maximum value of the experimental data at $z = 32$ cm. In our calculations, a uniform axial wavenumber estimated from the experimental data is assumed. In particular, the phase differences measured at two axial positions, φ_{rel1} and φ_{rel2}, are used to determine the axial wavenumber $k_{\|} = (\varphi_{rel2} - \varphi_{rel1})/(z_2 - z_1)$, where $z_1 = 0.1$ m and $z_2 = 0.34$ m. The blue dotted curves in Fig. 9 are drawn using the model equation (14) at various values of t. It can be seen from Fig. 9 that Eq. (14) (blue dotted lines) recovers the experimental data (red curve with red dots) in $z < 34.5$ cm fairly well. The slight difference between the results of the calculation and the experiment near the plasma terminating plate can be attributed to the effect of theoretically predicted surface waves.[24]

Outside the insulator plate ($z > 34.5$ cm), the excited rf magnetic field behaves like an evanescent wave generated in an ICP, whose e-folding decay length is ~ 1.8 cm corresponding to the skin depth including the collision effect.[32] The helicon wave cannot propagate into the region outside the insulator plate because the helicon dispersion relation cannot be satisfied in such a low density plasma there. As mentioned before (Fig. 8), it can be concluded that the plasma production is restricted in the left-hand side region of the insulator plate ($0 < z < 34.5$ cm).

In Figs. 10 and 11, the spatial and temporal behaviors of excited rf wave structures under various experimental conditions are shown. Twelve solid curves in each frame correspond to the spatial profiles of Eq. (13) at different t's during one rf period while the red curve with red dots correspond to the profiles of Eq. (13) at $t = 0$. The dots indicate the positions of measurements and the red curves are drawn in order to delineate the wave patterns. Figure 10 shows how the helicon wave structure $\tilde{B}_z/|\tilde{I}_A|$ changes as the effective plasma length is varied in low-aspect ratio plasmas. The experimental conditions are: $P_{inp} = 2 - 4$ kW and $z_E = 5.5$, 12.5, and 34.5 cm ($A \sim 0.075$, 0.17, and 0.47), respectively. For the cases of all kinds of boundaries, it is found that the axial mode number increases with the increase in z_E. We

TABLE I. Axial mode numbers and experimental conditions for Fig. 10

	$z_E = 5.5$ cm	$z_E = 12.5$ cm	$z_E = 34.5$ cm
Conductor plate with holes	(a): $n_{IC} \sim 1/4\ n_{ec} \sim 4.5 \times 10^{11}$ cm^{-3}	(b): $n_{IC} \sim 3/4\ n_{ec} \sim 6 \times 10^{11}$ cm^{-3}	(c): $n_{IC} \sim 5/4\ n_{ec} \sim 8 \times 10^{11}$ cm^{-3}
Conductor plate	(d): $n_{IC} \sim 1/4\ n_{ec} \sim 3 \times 10^{11}$ cm^{-3}	(e): $n_{IC} \sim 3/4\ n_{ec} \sim 1 \times 10^{12}$ cm^{-3}	(f): $n_{IC} \sim 7/4\ n_{ec} \sim 2 \times 10^{12}$ cm^{-3}
Insulator plate	(g): $n_{II} \sim 1/2\ n_{ec} \sim 7 \times 10^{11}$ cm^{-3}	(h): $n_{II} \sim 1/2\ n_{ec} \sim 4.5 \times 10^{11}$ cm^{-3}	(i): $n_{II} \sim 3/2\ n_{ec} \sim 4 \times 10^{12}$ cm^{-3}

summarize the axial mode numbers derived from Fig. 10 in Table I. The values of the electron density at the center of the plasma region ($x = 0$ cm and $z = z_E/2$), n_{ec}, are also shown in Table I. The results agree well with the axial mode numbers obtained using Eqs. (10) and (11). We can see that the amplitude of the helicon wave becomes zero at the conductor boundary [see Figs. 10(a)–10(f)]. On the other hand, as can be seen in Figs. 10(g)–10(i), the amplitude at the insulator boundary is slightly less than the local maximum.

How the axial profile of $\tilde{B}_z/|\tilde{I}_A|$ changes with the electron density at the center of the plasma region, n_{ec}, is shown in Fig. 11 for three different axial boundaries. The value of n_{ec} at $x = 0$ cm and $z = z_E/2$ is varied by adjusting the input rf power P_{inp}. The axial position of the plasma terminating plate is $z_E = 34.5$ cm ($A \sim 0.47$). The axial mode numbers estimated using the data shown in Fig. 11 are summarized in Table II. It can be seen that the axial mode numbers (the parallel wavenumbers) increase with the increase in the input rf power P_{inp} or the increase in n_{ec}. The behavior is similar to what one can expect from the helicon wave dispersion relation for an infinite cylindrical plasma immersed in a uniform magnetic field. In addition, the experimental results (not shown) show that the axial profiles of $\tilde{B}_z/|\tilde{I}_A|$ can be altered by changing the magnetic field configurations. The axial mode number (the axial wavenumber) increases with the decrease in the magnetic field strength. The behavior is also consistent with what one can expect from the helicon wave dispersion relation for an infinite cylindrical plasma immersed in a uniform magnetic field.

In Fig. 12, the electron density averaged over the z-axis at $x = 0$, $\bar{n}_e$, is plotted against the experimentally determined average parallel wavenumber $k_\parallel$ for the case of $z_E = 34.5$ cm ($A \sim 0.47$). The black squares and the blue triangles correspond to the data points for the cases of the conductor plate with holes and the solid insulator plate, respectively. The data were obtained with plasmas in the helicon discharge mode. When a plasma is produced in an inductively coupled mode, not in a helicon discharge mode, the observed rf fields are in an evanescent state. On the other hand, a plasma produced with the input power $P > P_{th}$ (the threshold power for the density jump) is always accompanied by a propagating wave activity which is helicon like along the axial direction as shown in Fig. 12. The solid curve shows the dispersion relation of helicon waves with $a = 21.5$ cm ($k_{\perp 1} = 0.18$ cm^{-1}) using Eq. (5). Here, as an effective plasma radius a, we adopt the radius of the flat spiral antenna (43 cm/2 = 21.5 cm). This is based on the fact that the full width at half maximum (FWHM) of measured radial electron density profiles in the case of a conductor plate with holes [see black squares in Fig. 6(a)] is ~43 cm.

In the cases of the conductor plate with holes and the solid insulator plate for $k_\parallel < 0.25$ cm^{-1} (for which the input rf power is relatively low), the experimental data lie on the helicon wave dispersion relation. On the other hand, the data for the case of the insulator plate with $k_\parallel > 0.3$ cm^{-1} deviate from the helicon wave dispersion relation with $k_{\perp 1} = 0.18$ cm^{-1}. This discrepancy is most likely due to the uncertainty in estimating the perpendicular wavenumber.

Figure 13 shows the radial profiles of the electron density [the first row of the figure: (a) and (d)], the amplitude of the excited rf magnetic field [the middle row of the figure: (b) and (e)], and the phase difference [the third row of the figure: (c) and (f)] for the case of the insulator plasma terminating plate. In the case of lower input power ($P_{inp} \sim 1$ kW) corresponding to the data of $(\bar{n}_e,\ k_\parallel) \sim (2.5 \times 10^{11}\text{cm}^{-3},\ \ 0.21\text{cm}^{-1})$ in Fig. 12, the radial profile of the electron density [Fig. 13(a)] is almost flat near the plasma center, and the amplitude [Fig. 13(b)] and the phase difference [Fig. 13(c)] of the excited rf magnetic field show a good agreement with those of an ideal helicon wave, $J_0(k_{\perp 1}x)$ for $k_{\perp 1} = 0.18$ cm^{-1}, obtained from Eq. (9). This result is consistent with the fact that the experimental data lie on the helicon wave dispersion relation as shown in Fig. 12.

In the case of a higher input rf power ($P_{inp} \sim 3$ kW) for the insulator boundary corresponding to the data of $(\bar{n}_e,\ k_\parallel) \sim (4.5 \times 10^{12}\,\text{cm}^{-3}, 0.42\,\text{cm}^{-1})$ in Fig. 12, the radial profiles of the electron density [Fig. 13(d)] and the amplitude of the excited rf magnetic field [Fig. 13(e)] become peaked. It is found that the helicon wave with the perpendicular wavenumber of $k_{\perp 2} = 7.02/a$ (Refs. 33–35 for $a = 21.5$ cm can well explain the observed wave amplitude [Fig. 13(e)] near the plasma central region. The phase difference data [Fig. 13(f)] also qualitatively agrees with the theoretical predictions (i.e., the phase difference increases from 0 to 360 in $x < 20$ cm). This result suggests that the helicon

TABLE II. Axial mode numbers and experimental conditions for Fig. 11.

	$P_{inp} \sim 1$ kW	$P_{inp} \sim 2$ kW	$P_{inp} \sim 4$ kW
Conductor plate with holes	(a): $n_{IC} \sim 3/4\ n_{ec} \sim 2 \times 10^{11}$ cm^{-3}	(b): $n_{IC} \sim 5/4\ n_{ec} \sim 4 \times 10^{11}$ cm^{-3}	(c): $n_{IC} \sim 5/4\ n_{ec} \sim 8 \times 10^{11}$ cm^{-3}
Conductor plate		(d): $n_{IC} \sim 5/4\ n_{ec} \sim 1 \times 10^{12}$ cm^{-3}	(e): $n_{IC} \sim 7/4\ n_{ec} \sim 2 \times 10^{12}$ cm^{-3}
Insulator plate	(f): $n_{II} \sim 1\ n_{ec} \sim 1 \times 10^{12}$ cm^{-3}	(g): $n_{II} \sim 3/2\ n_{ec} \sim 2 \times 10^{12}$ cm^{-3}	

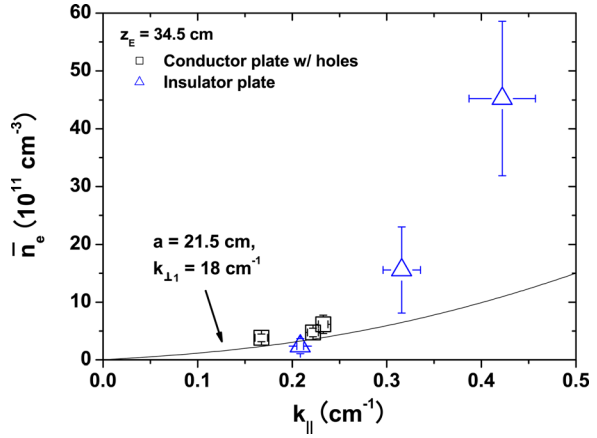

FIG. 12. Axially line averaged electron density $\bar{n}_e$ ($x = 0$ cm) plotted against the experimentally determined average parallel wavenumber $k_\parallel$ for low-aspect ratio helicon plasmas under different axial boundary conditions. The position of plasma terminating plate was at $z_E = 34.5$ cm ($A \sim 0.47$). The squares correspond to the data taken using a plasma terminating plate made of a conductor plate with small holes. The triangles correspond to the data taken using a plasma terminating plate made of a solid insulator plate. The solid curve is a result of the calculation based on the helicon wave dispersion relation for a uniform cylindrical plasma with a radius of $a = 21.5$ cm (corresponding to $k_{\perp 1} = 0.18$ cm^{-1}).

wave with higher perpendicular wavenumber might have been excited in the discharge regime with higher electron density. The effect of the non-uniform radial electron density profile presumably plays an important role in the helicon plasma production[36,37] as well.

V. CONCLUSIONS

Low-aspect ratio ($0.075 \leq A \leq 0.47$), high-density ($\gtrsim 10^{12}$ cm^{-3}) helicon plasmas with a large-diameter (73.8 cm) have been successfully generated under three different types of axial boundary conditions that are realized by using three different types of plasma terminating plates: (1) a conductor (stainless steel) plate with small holes, (2) a solid conductor (stainless steel) plate, and (3) a solid insulator (mica) plate.

Under all axial boundary conditions examined in our experiments, the "density jump" to mark the transition from an ICP to a helicon plasma (HP) has been observed even for the lowest aspect ratio case ($A \sim 0.075$ for $z_E = 5.5$ cm). A typical value of the electron density after the density jump is 10^{12}–10^{13} cm^{-3}. The discharge mode after the density jump ($n_e \gtrsim 10^{12}$ cm^{-3}) has been identified as a helicon-wave discharge through the observation of helicon waves in plasma.

In order to examine the utility of our low-aspect ratio helicon plasma device, we have determined the number of ion-electron pairs produced by unit input rf power, i.e., N_e/P_{inp}, a measure of the PPE. It has been found that the dominant plasma loss mechanism is the axial diffusion and the PPE does not depend on the character of the axial boundary. The PPE simply increases in proportion to the axial plasma length. For low-aspect ratio ($A \gtrsim 0.17$ for $z_E \gtrsim 12.5$ cm) helicon plasmas under all boundary conditions, the PPE is $\sim 2 \times 10^{12}$ W^{-1}. In order to retain the high PPE even in low-aspect ratio helicon plasmas, the use of a flat type antenna is advantageous because having a large-diameter plasma can be easily realized by simply making the antenna diameter larger. It can be concluded that our low-aspect ratio helicon plasma source is very useful for various plasma applications that require high plasma density of $\gtrsim 10^{12}$ cm^{-3}.

In order to understand the characteristics of helicon waves excited in our low-aspect ratio helicon plasmas, we have measured excited rf magnetic fields to examine the helicon wave structure. The observed waves are a standing wave type and the wave structures are strongly dependent of the nature of the axial boundary. Discrete axial wave modes have been experimentally determined, and the results are successfully interpreted by using a simple model under the assumption of a uniform axial wavenumber. The helicon

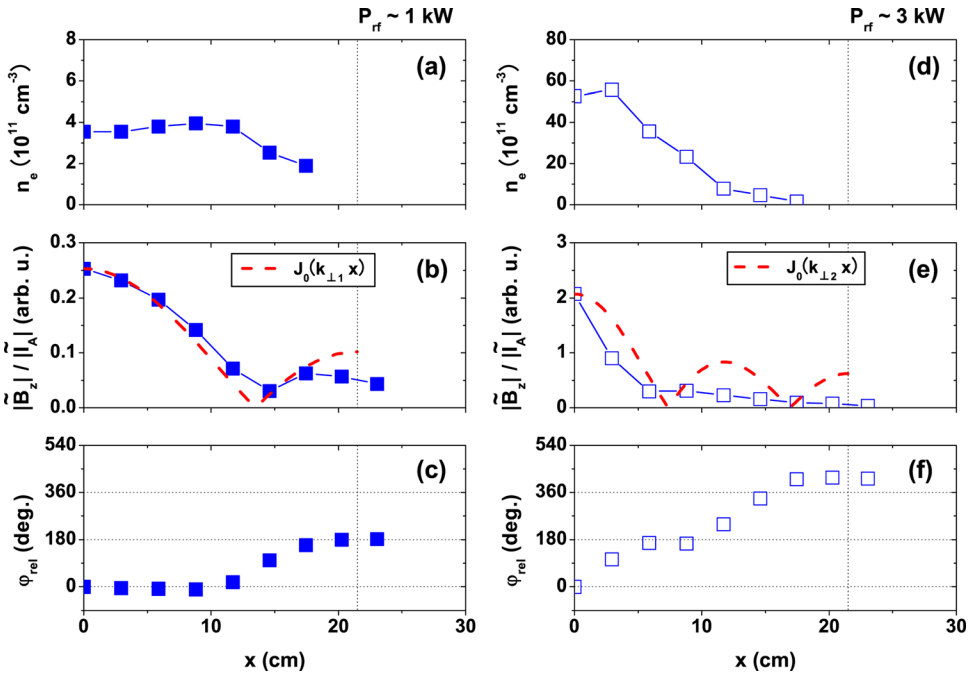

FIG. 13. Radial profiles of the electron density, n_e, [(a) and (d)], the excited rf magnetic field, $|\tilde{B}_z|/|\tilde{I}_A|$, [(b) and (e)], and the phase difference between the phase of $\tilde{B}_z$ and that of $\tilde{I}_A$ (the reference signal), φ_{rel}, [(c) and (f)] for low-aspect ratio ($A \sim 0.47$) helicon plasmas. The plasma terminating plate used was a solid insulator plate located at $z_E = 34.5$ cm. The input rf powers used were $P_{inp} \sim 1$ kW for (a) – (c) and $P_{inp} \sim 3$ kW for (d) – (f). The measurements were carried out at $z = 25$ cm for (a) – (c) and $z = 15$ cm for (d) – (f). The red dashed curves in (b) and (e) represent the Bessel functions $J_0(k_{\perp j} r)$ with $j = 1$ and $j = 2$, respectively.

wave dispersion relation, that includes the effect of a first order perpendicular wavenumber only, can well explain the characteristics of waves for $k_{\parallel} < 0.25\ \mathrm{cm}^{-1}$ (associated with relatively low density helicon plasmas). When the plasma terminating plate is an insulator and/or the plasma density is relatively high, the radial profiles of the electron density and the wave amplitude become peaked at the plasma center. Our analysis strongly suggests that the results can be explained by including the effects of higher perpendicular wavenumbers in the analysis of helicon waves.

ACKNOWLEDGMENTS

Our experiments were performed at ISAS/JAXA under their research collaboration program. We would like to acknowledge various assistances given by Dr. I. Funaki, Dr. S. Sato, Dr. T. Takeda, Professor K. Yamagiwa, Professor S. Sasaki, Professor T. Abe, and Dr. K. Ueno in carrying out the experiments. One of the authors (T. M.) wishes to express his great appreciation to Professor M. Y. Tanaka, Dr. K. Terasaka, and the members of Tanaka laboratory at Kyushu University for the discussion regarding this research. The research was partially supported by the Grants-in-Aid for Scientific Research (S) 21226019, (A) 17206084, (B) 20340163 and (C) 19540524 from the Japan Society for the Promotion of Science. One of the authors (T. M.) is the Research Fellow of the Japan Society for the Promotion of Science.

[1]R. W. Boswell, Phys. Lett. **33A**, 457 (1970).
[2]S. Shinohara, Jpn. J. Appl. Phys. **36**, 4695 (1997).
[3]R. W. Boswell and F. F. Chen, IEEE Trans. Plasma Sci. **25**, 1229 (1997).
[4]F. F. Chen and R. W. Boswell, IEEE Trans. Plasma Sci. **25**, 1245 (1997).
[5]S. Shinohara and A. Fujii, Phys. Plasmas **8**, 3018 (2001).
[6]J. Hanna and C. Watts, Phys. Plasmas **8**, 4251 (2001).
[7]C. Charles and R. W. Boswell, Appl. Phys. Lett. **82**, 1356 (2003).
[8]F. R. Chang Díaz, Sci. Am. **283**, 90 (2000).
[9]K. Toki, S. Shinohara, T. Tanikawa, and K. P. Shamrai, *Proceedings of the 40th AIAA/ASME/SAE/ASEE Joint Propulsion Conference 3935* (Fort Lauderdale, USA, 2004).
[10]T. Tsukada, H. Nogami, Y. Nakagawa, and E. Wami, Jpn. J. Appl. Phys. **33**, 4433 (1994).
[11]G. Giroult-Matlakowski, C. Charles, A. Durandet, R. W. Boswell, S. Armand, H. M. Persing, A. J. Perry, P. D. Lloyd, S. R. Hyde, and D. Bogsanyi, J. Vac. Sci. Technol. A **12**, 2754 (1994).
[12]P. K. Lowenhardt, B. D. Blackwell, R. W. Boswell, G. D. Conway, and S. M. Hamberger, Phys. Rev. Lett. **67**, 2792 (1991).
[13]S. Shinohara and T. Tanikawa, Rev. Sci. Instrum. **75**, 1941 (2004).
[14]T. Tanikawa and S. Shinohara, in *Proceedings of the 12th International Congress on Plasma Physics*, Nice, France, 2004, http://hal.archives-ouvertes.fr/hal-00002013/en/.
[15]S. Shinohara and T. Tanikawa, Phys. Plasmas **12**, 044502 (2005).
[16]T. Tanikawa and S. Shinohara, Thin Solid. Films **506–507**, 559 (2006).
[17]T. Motomura, K. Tanaka, S. Shinohara, T. Tanikawa, and K. P. Shamrai, J. Plasma Fusion Res. Ser. **8**, 6 (2009).
[18]S. Shinohara, T. Hada, T. Motomura, K. Tanaka, Tanikawa, K. Toki, Y. Tanaka, and K. P. Shamrai, Phys. Plasmas **16**, 057104 (2009).
[19]J. E. Stevens, M. J. Sowa, and J. L. Cecchi, J. Vac. Sci. Technol. A **13**, 2476 (1995).
[20]M. Nisoa, Y. Sakawa, and T. Shoji, Jpn. J. Appl. Phys. **38**, L777 (1999).
[21]F. F. Chen, Plasma Phys. Controlled Fusion **33**, 339 (1991).
[22]K. P. Shamrai and S. Shinohara, Phys. Plasmas **8**, 4659 (2001).
[23]K. P. Shamrai, Plasma Sources Sci. Technol. **7**, 499 (1998).
[24]K. P. Shamrai, S. Shinohara, V. F. Virko, G. S. Kirichenko, V. M. Slobodyan, and Yu. V. Virko, Plasma Phys. Controlled Fusion **47**, A307 (2005).
[25]J. Hopwood, Plasma Sources Sci. Technol. **1**, 109 (1992).
[26]P. A. Keiter, E. E. Scime, and M. M. Balkey, Phys. Plasmas **4**, 2741 (1997).
[27]V. F. Virko, K. P. Shamrai, G. S. Kirichenko, and Yu. V. Virko, Phys. Plasmas **11**, 3888 (2004).
[28]K. P. Shamrai and S. Shinohara, Thin Solid Films **506–507**, 555 (2005).
[29]S. Shinohara and K. Yonekura, Plasma Phys. Controlled Fusion **42**, 41 (2000).
[30]S. Shinohara and K. P. Shamrai, Plasma Phys. Controlled Fusion **42**, 865 (2000).
[31]F. F. Chen, Plasma Sources Sci. Technol. **7**, 458 (1998).
[32]S. Shinohara and Y. Kawai, Jpn. J. Appl. Phys. **35**, L725 (1996).
[33]H. Takeno, Y. Yasaka, O. Sakai, and R. Itatani, Nucl. Fusion **35**, 75 (1995).
[34]M. Light, I. D. Sudit, F. F. Chen, and D. Arnush, Phys. Plasmas **2**, 4094 (1995).
[35]Y. Sakawa, N. Koshikawa, and T. Shoji, Plasma Sources Sci. Technol. **6**, 96 (1997).
[36]K. Niemi and M. Krämer, Phys. Plasmas **15**, 073503 (2008).
[37]S. Cho and J.-G. Kwak, Phys. Plasmas **4**, 4167 (1997).